

# Microcavity Sensor Enhanced by Spontaneous Chiral Symmetry Breaking

Yi-Yi Li,<sup>1</sup> Qi-Tao Cao,<sup>1,\*</sup> Jin-hui Chen,<sup>2</sup> Xiao-Chong Yu,<sup>3</sup> and Yun-Feng Xiao<sup>1,4,5</sup>

<sup>1</sup>*State Key Laboratory for Mesoscopic Physics and Frontiers Science Center for Nano-optoelectronics, School of Physics, Peking University, Beijing 100871, China*

<sup>2</sup>*Institute of Electromagnetics and Acoustics, Xiamen University, Xiamen 361005, China*

<sup>3</sup>*Department of Physics and Applied Optics Beijing Area Major Laboratory, Beijing Normal University, Beijing 100875, China*

<sup>4</sup>*Collaborative Innovation Center of Extreme Optics, Shanxi University, Taiyuan 030006, China*

<sup>5</sup>*Peking University Yangtze Delta Institute of Optoelectronics, Nantong 226010, China*

(Received 28 April 2021; revised 11 August 2021; accepted 22 September 2021; published 12 October 2021)

An optical microcavity provides a prominent platform for single-nanoparticle detection with ultrahigh sensitivity. Recently, microcavity sensors working at the exceptional point have caught great attention due to their ability to enhance sensitivity, but suffer from simultaneously amplified noise. Here, we propose employing a nonlinear microcavity to enhance the sensitivity of single-nanoparticle detection based on spontaneous chiral symmetry breaking. It is found that sensors operating at the symmetry-breaking threshold experience a gigantic enhancement in sensitivity, which is caused by the square-root response to perturbation in a lossless microcavity. Through the analysis for a realistic microcavity, a 30-fold sensitivity enhancement is demonstrated by working at the threshold, and the enhancement is also confirmed by numerical simulation. Furthermore, the noise performance is analyzed to be superior in thermorefractive noise and quantum noise performance in comparison to a conventional microcavity-sensing scheme. Merging the spontaneous chiral symmetry-breaking effect with practical sensing applications, the results pave a universal way for high-performance microcavity sensing with enhanced sensitivity and reduced noise.

DOI: 10.1103/PhysRevApplied.16.044016

## I. INTRODUCTION

Single-nanoparticle detection plays an increasing role in applications such as biological and chemical sensing [1]. While various techniques, such as tunable resistive pulse sensing [2–4], nanoparticle-tracking analysis [5,6], and interferometric scattering microscopy [7–9], have grown mature, it is still challenging but desirable to push the detection limit of single nanoparticles down to nanometer size in a portable-scale device. Optical whispering-gallery-mode (WGM) microcavities, with the merit of ultrahigh- $Q$  factor, are widely used in chip-scale optical sensors for the detection of single nanoparticles [10–19]. Previous research in WGM microcavity sensors has demonstrated the superior sensitivity of detecting single molecules or even single ions, with an unprecedented molecular weight of 2.35 kDa [18,19]. In order to further improve the detection limit, much effort has been made to enhance sensitivity for small perturbation, including using a hybrid microcavity [20–22], an active microcavity, mode-locking techniques [23] and detecting mode-broadening signals. In particular, introduction of exceptional points (EPs) in

a non-Hermitian system improves the sensitivity to small perturbations to an unprecedented level [24–30], leading to the development of devices such as nanoparticle sensors [24,26,28], gyroscopes [29], and optomechanical sensors [30].

Although the sensitivity of EP microcavity sensors are proved to be enhanced theoretically and experimentally, with analysis of Hamiltonian dynamics [31,32], Fisher information [33–35] and Petermann factor [36], the quantum SNR performance of current EP microcavity sensors are calculated to be not improved because of the simultaneously magnified quantum noise. Besides the EPs with respect to parity-time symmetry breaking, another optical singularity caused by spontaneous chiral symmetry breaking (SCSB) [37] is recently observed experimentally in WGM microcavities [38,39]. When the intra-cavity intensity exceeds the threshold at the singularity, the counterpropagating clockwise (CW) and counterclockwise (CCW) waves inside the microcavity evolve into a chiral state due to the Kerr-effect-induced nonlinear coupling, with unbalanced intensities in CW and CCW directions. This spontaneous chiral symmetry breaking can lead to many phenomena and performance enhancement in a wide range of optical devices, such as sensors

\* caoqt@pku.edu.cn

[40–43], logic gates [44], switches [45,46], and nonreciprocity devices [47].

In this work, we propose employing a nonlinear microcavity to enhance the sensitivity of single-nanoparticle detection based on SCSB. When a tiny perturbation occurs in the evanescent field of the microcavity, the coupling strength between CW and CCW waves changes slightly, leading to a measurable contrast in the intensity of counterpropagating waves. It is further found that intensity difference response can be significantly enlarged near the SCSB threshold, with a square-root relationship to the external perturbation. Moreover, the SNR is analyzed and is compared with the backscattering-based sensing scheme, demonstrating a better performance in overcoming the thermorefractive noise and quantum noise.

## II. SENSITIVITY ANALYSIS

As shown in Fig. 1(a), the counterpropagating CW and CCW traveling waves in a microcavity can be intrinsically coupled due to the surface scattering and form a pair of standing-wave supermodes [48–50]. In the linear regime, the supermodes consist of equal intensity CW and CCW traveling waves and are distinguished by the phase difference between the counterpropagating waves. Specifically, the low- (high-) frequency symmetric (antisymmetric) supermode has a phase difference of 0 ( $\pi$ ) between the counterpropagating waves. When the Kerr nonlinearity effect is introduced, an intensity-dependent nonlinear coupling comes into force [Fig. 1(a)], where the evolution of CW and CCW modes  $a_{\text{cw}}$  and  $a_{\text{ccw}}$  can be described by the coupled-mode equations

$$\frac{da_m}{dt} = i\omega_c a_m + ig_0 a_{m'} + iM(|a_m|^2 + 2|a_{m'}|^2)a_m, \quad (1)$$

where  $m \neq m'$  stands for CW and CCW,  $\omega_c$  is the eigenfrequency of the waves,  $g_0$  is the intrinsic linear coupling strength, and  $M$  is a constant related to the Kerr nonlinearity of the cavity. The Kerr nonlinearity induces a self-phase modulation term  $iM|a_m|^2 a_m$  and a cross-phase modulation term  $2iM|a_{m'}|^2 a_m$ , where the cross-phase modulation is twice as strong as the self-phase modulation. By rewriting Eq. (1) (see Appendix 1), we can obtain the effective coupling between the counterpropagating waves  $g_{\text{eff}} = g_0 + Ma_{\text{ccw}}^* a_{\text{cw}}$ . As for the antisymmetric mode, when the intracavity intensity reaches the threshold  $A_{\text{th}}^2$ , the intrinsic coupling strength can be entirely compensated by the Kerr nonlinearity ( $g_{\text{eff}} = 0$ ), and the chiral symmetry of the counterpropagating optical field breaks spontaneously with a vanished frequency splitting between the supermodes [38]. Note that here the order parameter is conventionally defined as the chirality  $C = (|a_{\text{cw}}|^2 - |a_{\text{ccw}}|^2)/(|a_{\text{cw}}|^2 + |a_{\text{ccw}}|^2)$ . Beyond the threshold at the critical point [red star in Fig. 1(b)], two chiral states emerge randomly, corresponding to the two dashed branches in Fig. 1(b), and the

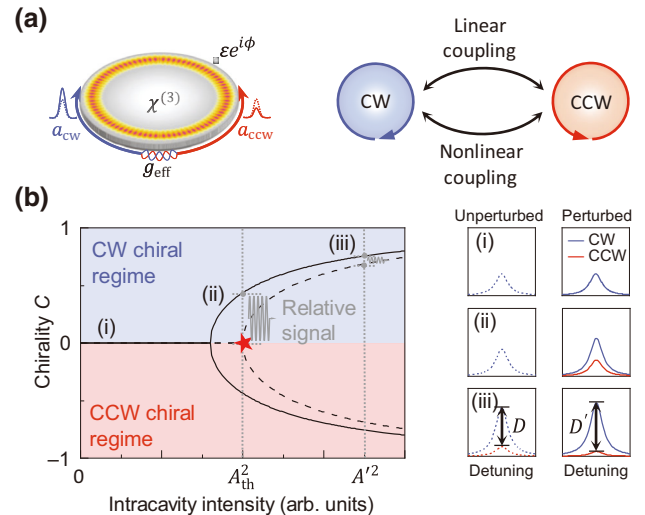


FIG. 1. (a) Schematic of the microcavity sensor enhanced by spontaneous chiral symmetry breaking. Left: visualization of the chiral optical field in a disk microcavity with  $\chi^{(3)}$  Kerr nonlinearity, where red and blue dashed curves represent the unperturbed CCW and CW traveling waves with an effective coupling strength of  $g_{\text{eff}}$ .  $\varepsilon e^{i\phi}$  is the perturbation induced by an attached nanoparticle, which changes the traveling waves into the chiral optical fields marked by solid curves. Right: coupling mechanism between CW and CCW waves. (b) The dashed (solid) curves show the dependence of the chirality  $C$  on the intracavity intensity  $A^2$  before (after) perturbation. (i)–(iii) The intensity of CCW and CW waves at different intracavity intensities.

CW-CCW intensity difference  $D = P_{\text{cw}} - P_{\text{ccw}}$  becomes larger with the increased intracavity intensity.

When a nanoparticle enters the evanescent field of the microcavity, an extra coupling is introduced by the scattering between CW and CCW waves, resulting in a perturbation to the linear coupling strength. Thus, the nanoparticle shifts the symmetry-breaking threshold and the CW-CCW intensity difference  $D$  can be changed, shown as the solid line in Fig. 1(b), so that the variation of the intensity difference  $\Delta D$  is used as the sensing signal. Compared to the case when the intracavity intensity  $A^2$  is away from threshold, the relative signal  $\Delta D/A^2$  [gray line in Fig. 1(b)] is significantly enhanced when the intracavity intensity is chosen at the symmetry-breaking threshold  $A_{\text{th}}^2$ , which leads to a greater sensitivity to perturbations. In the following subsections, we analyze the sensitivity enhancement first in a lossless microcavity in Sec. A, and then verify the results with consideration of a realistic lossy microcavity (Sec. B) and numerical simulation (Sec. C).

### A. Theoretical results with a lossless microcavity

We first consider a closed microcavity where the optical loss is neglected. The steady-state solutions of Eq. (1) demonstrate that the intensity difference of the CW (CCW)

waves is

$$D = \sqrt{A^4 - 4 \left(\frac{g_0}{M}\right)^2}, \quad (2)$$

where  $D$  becomes nonzero when the intracavity intensity  $A^2$  is greater than the threshold intensity  $A_{\text{th}}^2 = 2g_0/M$ . When a nanoparticle is attached to the microcavity, the real part of the perturbation for the linear coupling strength reads  $\varepsilon \cos(\phi)$  [51], where the phase  $\phi$  depends on the azimuthal position of the nanoparticle and would experience a change from 0 to  $\pi$  while the position of the analyte particle changes between adjacent antinodes.

In order to characterize the best performance with a max possible signal of this sensor, we take  $\phi = \pi$  as an example, and the variation in the CW-CCW intensity difference at the threshold  $A_{\text{th}}^2$  is expanded as  $\Delta D = \sqrt{8\varepsilon g_0/M^2}$  with  $\varepsilon \ll g_0$ , where the effective coupling strength remains zero as well as the modal splitting. It is found that this square-root response leads to the significant enhancement of sensitivity for small perturbations (Fig. 2). Note that the perturbation induced by an attached nanoparticle can also increase the initial linear coupling strength. To respond to such a positive perturbation strength, the sensor has to work at an intracavity intensity slightly higher than SCSB threshold.

The dependence of the sensing signal  $\Delta D$  on the intracavity intensity  $A^2$  and the perturbation strength  $\varepsilon$  is plotted in Fig. 2(a). When the intracavity intensity is lower than  $A_{\text{th}}^2 = 2$ , small perturbations do not break chiral symmetry and therefore the sensing signals are zero [gray zone in Fig. 2(a)], and the sensing signal emerges only for perturbation strength  $\varepsilon > g_0 - MA^2/2$ . Increasing the intracavity intensity to the threshold, the sensing signal reaches its maximum for any perturbation strength. Further increasing the intracavity intensity higher than  $A_{\text{th}}^2$ , the sensing signal starts to drop. This emphasizes that the signal magnification is induced by the emergence of the SCSB

singularity, but not the increase in the intracavity intensity. Specifically, the dependence of the sensing signal to perturbation at interfaces  $A^2 = 1.5, 2, 2.5$  in Fig. 2(a) is illustrated in Fig. 2(b). The sensing signal at threshold intensity  $A_{\text{th}}^2 = 2$  is enhanced for all perturbation strength.

Moreover, the response of the signal to small perturbation in the logarithm plot exhibits a slope of  $1/2$  at  $A_{\text{th}}^2 = 2$ , confirming the square-root response given by the theory. In contrast, the signal has no response to small perturbations at lower intensity  $A^2 = 1.5$  and linear responses to small perturbations at higher intensity  $A^2 = 2.5$ . This square-root response at SCSB threshold  $A_{\text{th}}^2$  leads to enhancement in the sensitivity  $\Delta D/\varepsilon$  for small perturbations, which can be seen in Fig. 2(c). In contrast to sensors operating away from threshold intensity, the sensitivity is enhanced when the intracavity intensity is at threshold  $A_{\text{th}}^2$  [red line in Fig. 2(c)]. For small perturbation  $\varepsilon \rightarrow 0$ , the sensitivity at  $A_{\text{th}}^2 = 2$  is trended to infinity under the lossless model.

## B. Theoretical results with a lossy microcavity

In a realistic microcavity with coupling loss and intrinsic loss, the sensitivity of the single-particle detection is analyzed based on the add-drop structure shown in Fig. 3(a). Continuous-wave input light is evanescently coupled to the microcavity from a bus waveguide to excite cavity modes, and the counterpropagating output waves are separately collected through a drop waveguide. Note that here in order to excite the antisymmetric mode, the input light is injected bidirectionally with the same intensity  $P_{\text{in}}$  and a phase difference of  $\pi$ . The output spectra collected with a frequency down scan demonstrate the SCSB phenomenon. As shown in Fig. 3(a), under the configuration of Appendix 2, when the input intensity is lower than the SCSB threshold power of  $95 \mu\text{W}$ , the CW and CCW output spectra have a triangularlike shape due to the mode shift induced by Kerr nonlinearity, while their intensities remain the same. When

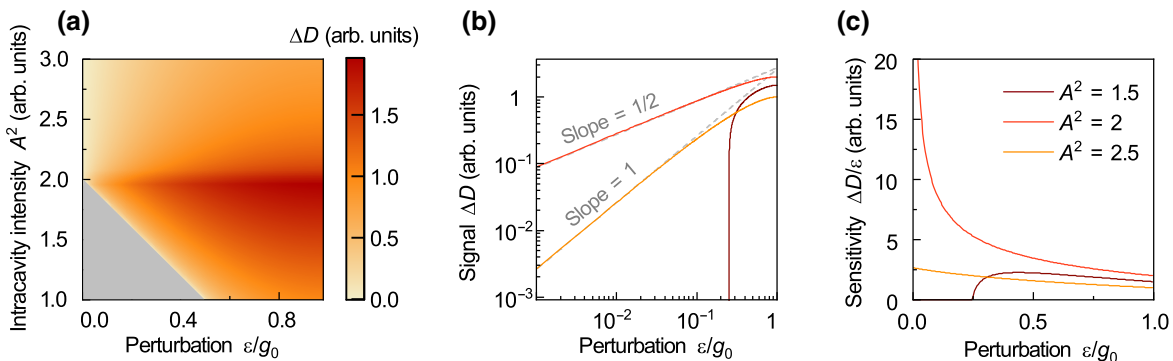


FIG. 2. Sensing analysis in a lossless microcavity. (a) The response of the signal  $\Delta D$  to the perturbation strength  $\varepsilon/g_0$  and the intracavity intensity  $A^2$ . The gray zone represents  $\Delta D = 0$ . (b) A logarithmic plot of the relationship between  $\Delta D$  and  $\varepsilon/g_0$  at intracavity intensities  $A^2 = 1.5, 2, 2.5$ . The gray dashed lines are linear fitting functions for perturbations  $\varepsilon/g_0 < 0.01$ . (c) The response of the sensitivity  $\Delta D/\varepsilon$  to the perturbation strength  $\varepsilon/g_0$  at  $A^2 = 1.5, 2, 2.5$ . The intensities are normalized by  $g_0/M$ .

the input intensity is higher than the threshold, the anti-symmetric mode field randomly falls into the CW or CCW chiral state and the counterpropagating wave intensities become unbalanced.

The dependence of the sensing signal  $\Delta D$  on the input power  $P_{\text{in}}$  and the intrinsic coupling strength  $g_0$ , shown in Figs. 3(b) and 3(c), demonstrates the sensing-signal enhancement at the SCSB threshold. For a certain linear coupling strength  $g_0$ , the sensing signal  $\Delta D$  reaches a peak at the threshold  $P_{\text{in,th}}$ . As the linear coupling strength  $g_0$  increases, the SCSB threshold raises accordingly, and the signal  $\Delta D$  is further enhanced around the threshold. As shown in Fig. 3(c), the SCSB threshold input power is demonstrated in the gray dashed line and matches with the peak of the sensing signal, confirming the signal is enhanced by SCSB effect. For a perturbation as small as  $\varepsilon/2\pi = 0.05$  MHz (approximately a polystyrene nanoparticle with a radius of 10 nm [52]), the output signal  $\Delta D$  can be magnified to more than 1  $\mu\text{W}$  at threshold  $P_{\text{in}} = 95.3 \mu\text{W}$ , which is strong enough for commonly used detectors to discriminate. The sensitivity enhancement is calculated to be 30 times larger than a sensor working at 200  $\mu\text{W}$ , where the sensing signal linearly responses to the perturbation as in many other microcavity-sensing schemes. The dependence of the output signal  $\Delta D$  on the perturbation strength  $\varepsilon$  is further calculated at the SCSB threshold ( $g_0/2\pi = 4.5$  MHz and  $P_{\text{in}} = 95.3 \mu\text{W}$ ) [Fig. 3(d)]. The sensing-signal response to the perturbation is fitted with a power function, exhibiting a relationship of  $\Delta D \propto \varepsilon^{0.65}$ , where the sensitivity  $\Delta D/\varepsilon$  is confirmed to be enhanced for small perturbation. The sensing-signal response varies from a square-root response due to the loss of the system.

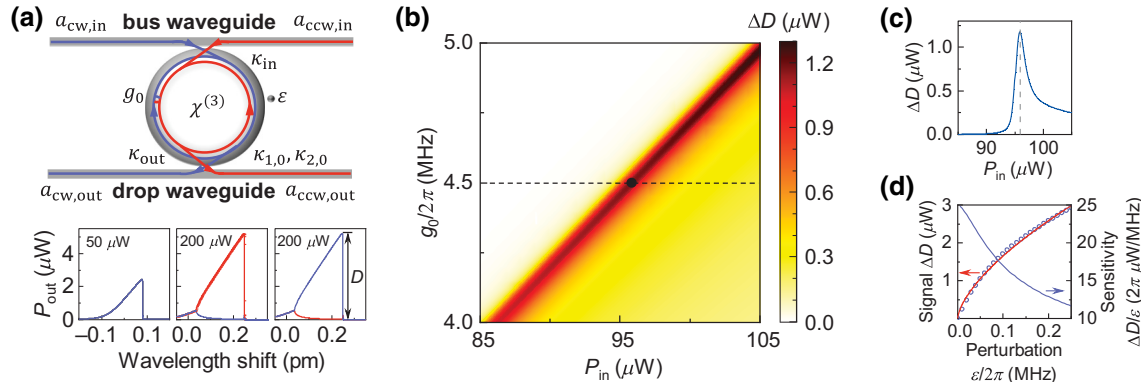


FIG. 3. (a) Top: a lossy microcavity sensor with an add-drop coupling structure. The red (blue) curve represents the CCW (CW) wave. A nanoparticle attached to the cavity induces an extra coupling strength  $\varepsilon$ . Bottom: typical drop-port spectra with input power  $P_{\text{in}}$  of 50 and 200  $\mu\text{W}$  from each port of the bus waveguide. (b) Dependence of the output signal  $\Delta D$  on the input power  $P_{\text{in}}$  and the linear coupling strength  $g_0$ , under a perturbation strength of  $\varepsilon/2\pi = 0.05$  MHz. (c) The output signal  $\Delta D$  versus the input power at the intrinsic coupling strength of  $g_0/2\pi = 4.5$  MHz, corresponding to the dashed line in (b). (d) Dependence of the output signal  $\Delta D$  and the sensitivity  $\Delta D/\varepsilon$  on the perturbation strength  $\varepsilon$  at the chiral symmetry-breaking threshold. The blue dots are the signal from calculation and the red line is a fitting curve with a power function, and the blue line is the calculated sensitivity. The experimental adaptable parameters used in this calculation are  $\kappa_{1,0}/2\pi = \kappa_{2,0}/2\pi = 2.8$  MHz,  $\kappa_{\text{in}} = \kappa_{\text{out}} = 0.2\kappa_{1,0}$ ,  $M = 1.33 \times 10^{13}$  MHz/J.

### C. Numerical simulation results

The SCSB enhanced sensing scheme can be experimentally carried out in a silica microtoroid resonator under continuous-wave input, where the SCSB effect is observed [38]. Since Kerr nonlinearity is a universal effect, the SCSB enhanced sensing is a versatile scheme adaptable to microcavities of many materials, such as silicon nitride [53], and various geometries, including microspheres [54], microring resonators [53], and even fiber resonators [55]. Based on the proposed setup, we conduct a numerical simulation by the finite-element method (FEM) to further confirm this theoretical model. Considering the computing resources, we adopt a two-dimensional (2D) circular silica microcavity with a radius of 3.5  $\mu\text{m}$ , which is side coupled with two waveguides, similar to the setup in Fig. 3(a) (see Appendix B). Here due to the large radiation loss of a small cavity ( $Q \sim 10^5$ ), the intrinsic linear coupling strength  $g_0 = 25.7$  GHz is initially set much larger than the value in the theoretical model. To avoid the random emergence of the chiral states, two-sided anti-symmetric input is coupled to the resonator with a 10% bias in the CW input power to drive the system to the CW chiral state [38]. Nanoparticles with a radius of a few nanometers are placed near the surface of the cavity to induce a perturbation  $\varepsilon$  to the linear coupling strength. The typical output spectra before and after perturbation near the SCSB threshold are shown in Fig. 4(a), where the change of the intensity difference at the resonance frequency demonstrates that the perturbation has broken the chiral symmetry.

In the absence of a nanoparticle perturbation, the CW-CCW intensity difference  $D$  is shown as the dark blue dots in Fig. 4(b). With increase of the input power,  $D$  barely

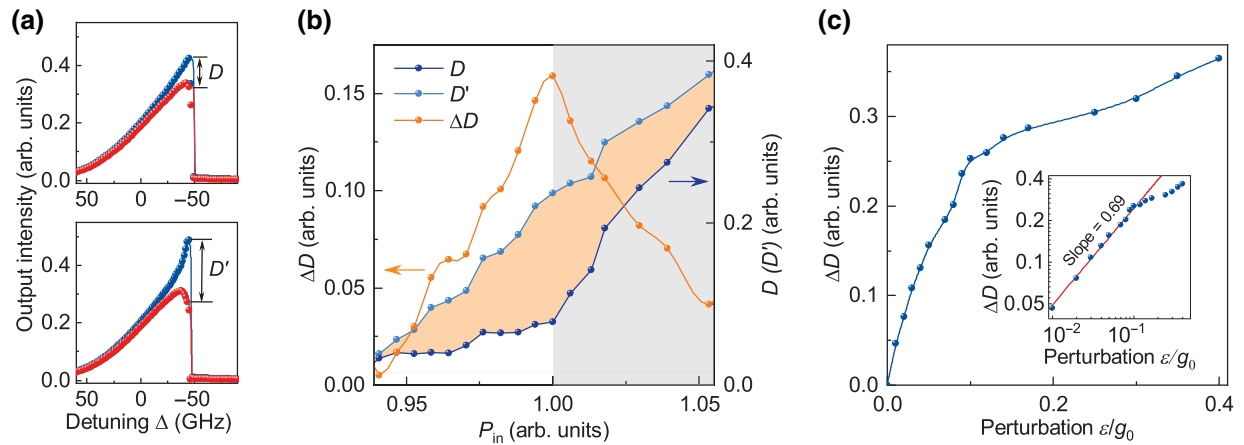


FIG. 4. Sensitivity analysis with two-dimensional numerical simulation results. (a) Output spectra obtained during the frequency scanning before (top) and after (bottom) perturbation. The dots and lines are simulation results and theoretical fitting, respectively. (b) The dependence of the intensity difference between CW and CCW outputs before ( $D$ , dark blue) and after perturbation ( $D'$ , light blue) on the input power  $P_{\text{in}}$  under a perturbation strength of  $\varepsilon/g_0 = 0.05$ . The sensing signal  $\Delta D$  is denoted in the orange dots. (c) Plots of the signal  $\Delta D$  versus the perturbation strength  $\varepsilon$  at the SCSB threshold in linear coordinate and logarithm coordinate (inset). Output intensity results are normalized by the input intensity and the perturbation  $\varepsilon$  is normalized by  $g_0$ .

changes below the SCSB threshold (white regime) and increases rapidly beyond threshold (gray regime), corresponding to the symmetry-breaking effect. Perturbed by a nanoparticle placed near the wave node of the original optical field distribution, the intensity difference  $D'$  changes into the light blue dots in Fig. 4(b). The sensing signal  $\Delta D$ , illustrated by orange dots, reaches a peak at the SCSB threshold. At the chiral symmetry-breaking threshold, the sensing signal  $\Delta D$  responses to the perturbation strength  $\varepsilon$  with a nonlinear behavior [Fig. 4(c)]. The signal response to the perturbation with a slope of 0.69 for small perturbations ( $\varepsilon < 0.1g_0$ ) in the logarithm plot, which demonstrates sensitivity enhancement compared to linear response.

### III. NOISE ANALYSIS

So far we prove the sensitivity enhancement of a nonlinear microcavity sensor working at the SCSB threshold. Furthermore, we investigate the noise performance of this sensor to demonstrate its validity. Analysis of the noise behavior is carried out with comparison to the backscattering-based sensor [13], which has been demonstrated with a prominent SNR among various microcavity-sensing schemes.

In order to deal with the nonlinear system, we separate the output intensity to its mean value  $\bar{D}$  and its fluctuation  $\delta D$ , which is widely adopted in the analysis of a backscattering-based sensor [13]:

$$D = \bar{D} + \delta D. \quad (3)$$

The output intensity  $\bar{D}$  is calculated by neglecting the noise terms, and the fluctuation of the output intensity

$\delta D$  is calculated by expanding the nonlinear coupled-mode equations to the first order of the fluctuation terms (see Appendix 2). We analyze the frequency noise spectrum of the sensing signal  $\langle |\delta(\Delta D)|^2 \rangle(\omega)$  and calculate its dependence on the noise spectrum of different noise sources:

$$\begin{aligned} \langle |\delta(\Delta D)|^2 \rangle(\omega) = & c_{\text{th}}(\omega)S_{\text{th}}(\omega) + c_{\text{RIN}}(\omega)P_{\text{in}}S_{\text{RIN}}(\omega) \\ & + c_{\xi}(\omega)P_{\text{in}}S_{\xi}(\omega) + c_q, \end{aligned} \quad (4)$$

where  $S_{\text{th}}(\omega)$  is the thermorefractive noise spectrum,  $S_{\text{RIN}}(\omega)$  and  $S_{\xi}(\omega)$  are the power spectrum of the relative intensity noise and relative phase noise of the input laser. The coefficients  $c_{\text{th}}(\omega)$ ,  $c_{\text{RIN}}(\omega)$ ,  $c_{\xi}(\omega)$ , and  $c_q$  demonstrate the dependence of the noise spectrum of the sensing signal on different noise sources, where  $c_q$  represents quantum noise. To analyze the noise level compared with the signal, we define parameters  $\sqrt{c_{\text{th}}}/\Delta D$ ,  $\sqrt{P_{\text{in}}c_{\text{RIN}}}/\Delta D$ ,  $\sqrt{P_{\text{in}}c_{\xi}}/\Delta D$ , and  $\sqrt{c_q}/\Delta D$ , and they characterize the relative noise dependence of the signal on the thermorefractive noise, laser-intensity noise, laser-phase noise, and quantum noise. Here the noise spectrum of different noise sources  $S_{\text{th}}(\omega)$ ,  $S_{\text{RIN}}(\omega)$ , and  $S_{\xi}(\omega)$  are not included in the comparison because they are irrelevant to the sensing method used and remain the same as long as the sensing device is unchanged.

Although  $c_{\text{th}}, c_{\text{RIN}}, c_q$  are related to the noise frequency  $\omega$ , the calculation is carried out in the realistic limit of  $\omega \ll \kappa$ . However, the frequency dependence of  $c_{\xi}$  cannot be neglected and is demonstrated in Fig. 5(d). For both sensing schemes (the nonlinear effect is ignored in the backscattering case), the calculation is carried out with the same parameters as in Fig. 3 at  $g_0/2\pi = 5.835$

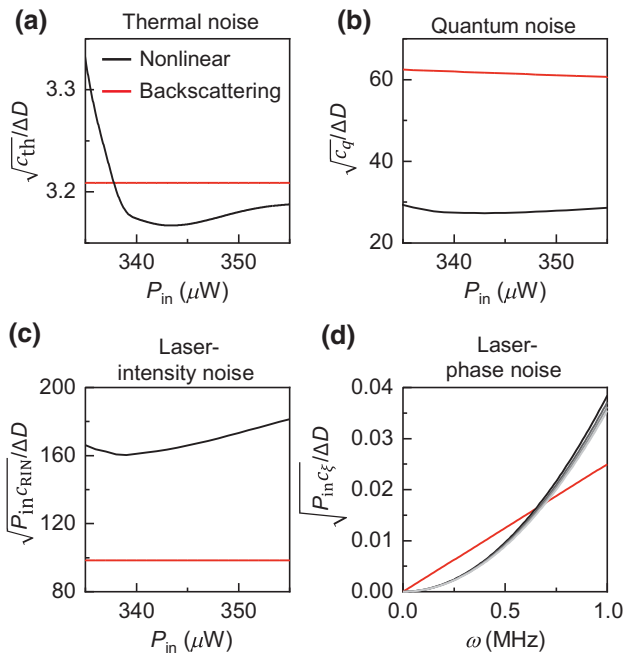


FIG. 5. Relative noise level compared to the signal. (a) Thermorefractive noise. (b) Quantum shot noise. (c) Relative laser-intensity noise. (d) Relative laser-phase noise. The black lines represent the proposed sensing method in this work, and the red lines represent the sensing method based on directly detecting backscattering intensities. The gradient gray curve in (d) covers the calculation from  $P_{\text{in}} = 335$  to  $355 \mu\text{W}$ , where the top curve represents  $P_{\text{in}} = 335 \mu\text{W}$ .

MHz, with only input from the CW side. The detuning is taken to be zero for the backscattering-based sensor to suppress laser-phase noise. It is shown that the nonlinear-based sensing scheme has a better behavior in overcoming thermorefractive noise near threshold in Fig. 5(a). For all of the intensities calculated, the nonlinear-based sensing scheme has a better performance in suppressing quantum noise, while the backscattering-based sensing scheme has a better performance in suppressing laser-intensity noise, as shown in Figs. 5(b) and 5(c). At low noise frequency (below 0.6 MHz in the given parameters), an improvement in the laser-phase noise performance is shown for the SCSB-enhanced sensing scheme [Fig. 5(d)]. The noise performance improvement can be understood by the self-referencing property of the CW-CCW intensity difference. The results confirm the advantage of using the SCSB-enhanced sensing scheme when the SNR is not limited by laser-intensity jitters. Compared to the EP-enhanced sensor, using the SCSB-enhanced sensing scheme has the potential to enhance sensitivity as well as suppress quantum noise.

#### IV. CONCLUSION

In conclusion, we propose and demonstrate theoretically an optical microcavity-sensing scheme working at the

chiral symmetry breaking threshold. With theoretical analysis and numerical simulation, we find that for sufficiently small perturbation, the sensing-signal responses to the perturbation with a power function at the chiral symmetry-breaking threshold, which magnifies the sensitivity. Furthermore, with comparison to the backscattering-based sensing scheme, the noise performance of low-frequency laser-phase noise, thermorefractive noise and quantum noise is proved to be enhanced. Compared to the EP-enhanced sensor, these results pave the way for an intensity-detection-based optical sensor to enhance sensitivity as well as noise performance. Since Kerr nonlinearity is a universal effect, the SCSB-enhanced sensing scheme can be widely adapted in all materials and microcavity structures. Aside from single-nanoparticle sensing, SCSB-enhanced sensing can be used to enhance the sensitivity of many other physical quantities, and could be widely applied in biological sensing, environmental monitoring, and rotation sensing.

#### ACKNOWLEDGMENTS

The authors thank Y.-J. Qian for helpful discussions. This project is supported by Key R&D Program of Guangdong Province (Grant No. 2018B030329001), the National Natural Science Foundation of China (Grants No. 11825402, No. 11654003, No. 12174010, No. 12104059, and No. 62005231). Q.-T. Cao is supported by the National Postdoctoral Program for Innovative Talents (Grant No. BX20200014) and China Postdoctoral Science Foundation (Grant No. 2020M680185). X.-C. Yu is supported by the Fundamental Research Funds for the Central Universities. Y.-Y. Li is supported by the China College Innovation Training Program.

#### APPENDIX A: COUPLED-MODE EQUATIONS

##### 1. Lossless coupled-mode equations

The electric fields of the two standing-wave supermodes are assumed to be  $\mathbf{E}_{1,2}(\mathbf{r}, t) = a_{1,2}(t)\mathbf{A}_{1,2}(\mathbf{r})e^{(i*\omega_{1,2}*t)}$ , where  $\omega_{1,2}$  are the eigenfrequencies of the two standing-wave supermodes.  $\mathbf{A}_{1,2}(\mathbf{r})$  are the normalized spacial part of the high-frequency and low-frequency supermodes and  $a_{1,2}(t)$  are the state amplitudes. Changing to the CW-CCW mode basis  $a_{\text{cw}} = (a_1 + ia_2)/\sqrt{2}$  and  $a_{\text{ccw}} = (a_1 - ia_2)/\sqrt{2}$ , the coupled-mode equation, Eq. (1), in the main text can be written into

$$\begin{cases} \frac{da_{\text{cw}}}{dt} = i\omega_c a_{\text{cw}} + ig_{\text{eff}}^* a_{\text{ccw}} + iM(|a_{\text{cw}}|^2 + |a_{\text{ccw}}|^2)a_{\text{cw}} \\ \frac{da_{\text{ccw}}}{dt} = i\omega_c a_{\text{ccw}} + ig_{\text{eff}}^* a_{\text{cw}} + iM(|a_{\text{ccw}}|^2 + |a_{\text{cw}}|^2)a_{\text{ccw}} \end{cases}, \quad (\text{A1})$$

where  $g_{\text{eff}} = g_0 + Ma_{\text{ccw}}^* a_{\text{cw}}$  is the effective coupling coefficient, and  $g_0$  is the linear coupling strength,  $M = 2\omega_c \chi^{(3)} / (\varepsilon_0 n^4 V_m) \propto \chi^{(3)}$  is a constant related to the Kerr

nonlinearity of the cavity, where  $n$  is the refractive index of the material,  $\varepsilon_0$  is the vacuum dielectric constant, and  $V_m$  is the second-order mode volume

$$V_m = \left[ \int \left( \frac{\varepsilon_0 n^2}{2} \mathbf{A}_{\text{cw}} \cdot \mathbf{A}_{\text{cw}}^* \right)^2 d^3 \mathbf{r} \right]^{-1} \quad (\text{A2})$$

and  $\mathbf{A}_{\text{cw}}(\mathbf{r})$  is the normalized spacial part of the CW eigenmode electric field.

The CW and CCW waves are parametrized with Bloch-sphere parameters

$$\begin{cases} a_{\text{cw}} = A e^{i\alpha} \cos \frac{\theta}{2} \\ a_{\text{ccw}} = A e^{i\alpha} \sin \frac{\theta}{2} e^{i\phi} \end{cases}, \quad (\text{A3})$$

where  $0 \leq \theta \leq \pi$ ,  $0 \leq \phi \leq 2\pi$ , and  $A e^{i\alpha}$  is the intracavity complex amplitude. The steady-state solutions of Eq. (1) show that the intensity of CW (CCW) waves  $|a_{\text{cw}}|^2$ ,  $|a_{\text{ccw}}|^2$  are the two distinct roots of the quadratic equation

$$(|a|^2)^2 - A^2 |a|^2 + \left( \frac{g_0}{M} \right)^2 = 0. \quad (\text{A4})$$

When the intracavity intensity  $A^2 \geq 2g_0/M$ , Eq. (A4) has two different real roots  $|a|_{\pm}^2 = A^2/2 \pm \sqrt{(A^2/2)^2 - (g_0/M)^2}$ , corresponding to the different intensities of the two counterpropagating waves, respectively. The intensity difference of the CW (CCW) waves is

$$D = |a|_+^2 - |a|_-^2 = \sqrt{A^4 - 4\left(\frac{g_0}{M}\right)^2}, \quad (\text{A5})$$

which is the same as Eq. (2).

At the threshold  $A_{\text{th}}^2$ , the sensing signal corresponding to a perturbation  $\varepsilon$  can be calculated by taking the difference in  $D$  before and after perturbation. When  $\varepsilon \ll g_0$ , the sensing signal at threshold can be expanded into a square-root response function

$$\begin{aligned} \Delta D &= \sqrt{A_{\text{th}}^4 - 4 \left( \frac{g_0 - \varepsilon}{M} \right)^2} - \sqrt{A_{\text{th}}^4 - 4 \left( \frac{g_0}{M} \right)^2} \\ &\approx A_{\text{th}}^2 \sqrt{2\varepsilon/g_0} \end{aligned} \quad (\text{A6})$$

as given in the main text. Note that here the perturbation changes the steady-state solution of the CW and CCW intensities, such that the perturbation will not be eliminated by nonlinear stabilizing effects such as mode locking or gain spiking [56].

## 2. Lossy coupled-mode equations

The considered open system is characterized by coupled-mode equations with loss, detuning and input

terms:

$$\begin{aligned} \frac{da_m}{dt} &= -\frac{\kappa_1}{2} \frac{a_m + a_{m'}}{2} - \frac{\kappa_2}{2} \frac{a_m - a_{m'}}{2} \\ &\quad + i\Delta_{\text{in}} a_m + ig_0 a_{m'} + iM(|a_m|^2 + 2|a_{m'}|^2) a_m \\ &\quad + \sqrt{\kappa_{\text{in}}} a_{m,\text{in}}, \end{aligned} \quad (\text{A7})$$

where  $m \neq m'$  stands for CW and CCW,  $\kappa_\mu = \kappa_{\mu,0} + \kappa_{\text{in}} + \kappa_{\text{out}}$  ( $\mu = 1, 2$ ) are the decay rates of the symmetric mode and the antisymmetric mode,  $\Delta_{\text{in}}$  is the detuning of the input laser.

The output signal can be calculated with the input-output relations:

$$a_{m,\text{out}} = -\sqrt{\kappa_{\text{out}}} a_m. \quad (\text{A8})$$

## APPENDIX B: SIMULATION METHODS

In the two-dimensional FEM simulation with COMSOL Multiphysics, the setup is similar to Fig. 3(a), where a circular silica microcavity with a radius of  $3.5 \mu\text{m}$  is side coupled with two silica waveguides. The waveguides have a  $0.3 \mu\text{m}$  width and the gap between the waveguide and the cavity edge is  $0.5 \mu\text{m}$ . To introduce linear coupling, two 30-nm-radius silica nanoparticles are placed symmetrically at the near field of the cavity. The perturbation is introduced by symmetrically placing silica nanoparticles with a radius of  $R_\varepsilon$ . Here the nanoparticles are placed symmetrically to reduce the effect of mesh asymmetry. The perturbation strength  $\varepsilon$  can be calculated by  $\varepsilon/g_0 = \alpha(R_\varepsilon)/\alpha(R_{g_0}) \cdot f^2(\vec{r}_\varepsilon)/f^2(\vec{r}_{g_0})$ , where  $\alpha(R) \propto R^2$  is the polarizability of the circular nanoparticle and  $f^2(\vec{r})$  represents the normalized distribution of the electrical field magnitude at the location  $\vec{r}$  of the nanoparticle [11]. In the simulation, all the nanoparticles are placed at wave nodes with a 80-nm gap between the nanoparticles and the cavity edge such that  $f^2(\vec{r})$  are the same for all nanoparticles. Therefore, the induced perturbation strength  $\varepsilon/g_0 = (R_\varepsilon/30 \text{ nm})^2$  can be controlled by changing the radius  $R_\varepsilon$  of the additional nanoparticles.

In order to simulate this SCSB effect, we build a computational model based on the nonlinear Maxwell equation for one component of the electrical field  $E(\mathbf{r}, t) = u(\mathbf{r}, t) e^{-i\omega t}$ . Under the slow-varying envelope approximation  $|\partial^2 u / \partial t^2| \ll \omega |\partial u / \partial t|$ , the equation reads

$$-2in^2 \frac{\omega}{c_0^2} \frac{\partial u}{\partial t} = \nabla^2 u + \frac{(n^2 + \chi^{(3)}|u|^2)\omega^2}{c_0^2} u. \quad (\text{B1})$$

where  $c_0$  is the speed of light. By adding an energy flux at both sides of the bus waveguide, bidirectional continuous-wave input is coupled to the resonator around the cavity resonant wavelength at 695 nm. The phase difference of the CW and CCW input light is set to  $\pi$  to drive the system into the antisymmetric supermode and a 10% bias is added

in the CW input side to drive the system into the CW chiral state. The output spectra are collected from the drop waveguide with frequency down scan. From the output spectra without nonlinearity, we obtain the linear coupling strength  $g_0 = 25.7$  GHz, the loss rates  $\kappa_1 = 25.5$  GHz and  $\kappa_2 = 23.8$  GHz.

## APPENDIX C: NOISE ANALYSIS

### 1. Introduction of the backscattering-based sensing scheme

In the backscattering-based sensing scheme, the input light is coupled to the cavity from the CW port of the drop waveguide, and the output backscattering light is detected from the same port of the waveguide. Neglecting nonlinearity, the system can be described by

$$\begin{aligned} \frac{da_m}{dt} = & -\frac{\kappa_1}{2} \frac{a_m + a_{m'}}{2} - \frac{\kappa_2}{2} \frac{a_m - a_{m'}}{2} \\ & + i\Delta_{\text{in}}a_m + ig_0a_{m'} + \sqrt{\kappa_{\text{in}}}a_{m,\text{in}}, \end{aligned} \quad (\text{C1})$$

where  $a_{\text{ccw,in}} = 0$ . The backscattering intensity is  $P_{\text{back}} = \kappa_{\text{in}}|a_{\text{ccw}}|^2$ , and the sensing signal is the change in the backscattering intensity before and after perturbation  $\Delta P_{\text{back}}$ .

### 2. Details of noise analysis

To analyze the noise of the SCSSB enhanced sensor, we first add all the considered fluctuation terms into the coupled-mode equations

$$\begin{aligned} \frac{da_m}{dt} = & -\frac{\kappa}{2}a_m + i(\Delta_{\text{in}} + g_{\text{th}}^s)a_m \\ & + i(g_0 + R_{\text{th}}^c \pm iI_{\text{th}}^c)a_{m'} + iM(|a_m|^2 + 2|a_{m'}|^2)a_m \\ & + \sqrt{\kappa_{\text{in}}}a_{m,\text{in}} + \sqrt{\kappa_l}\delta a_l + \sqrt{\kappa_{\text{out}}}\delta a_{m,\text{out}}, \end{aligned} \quad (\text{C2})$$

where  $m \neq m'$  stands for CW and CCW. Here we assume  $\kappa_1 = \kappa_2 = \kappa$ ,  $\kappa_l = \kappa - \kappa_{\text{in}} - \kappa_{\text{out}}$ . The terms  $g_{\text{th}}^s, g_{\text{th}}^c = R_{\text{th}}^c + iI_{\text{th}}^c$ , are the zero-mean fluctuations induced by thermorefractive noise, and their variances can be described by

$$S_{\text{th}} = \langle g_{\text{th}}^s \rangle = 2 \langle I_{\text{th}}^c \rangle = 2 \langle R_{\text{th}}^c \rangle. \quad (\text{C3})$$

As described in the main text, we separate the optical operators  $a$  into its mean value  $\alpha$  and its fluctuation  $\delta a$ , where  $a = \alpha + \delta a$ . The terms  $\delta a_l, \delta a_{m,\text{out}}$  are the zero-mean vacuum noise input terms. By breaking each input term into its amplitude  $X$  and phase  $Y$  quadratures as  $a = (X + iY)/2$ , all of the input terms contribute to the quantum noise due to the uncertainty principle. Assuming a coherent light input, the variance  $\langle \delta X_{\text{input}}^2 \rangle = \langle \delta Y_{\text{input}}^2 \rangle = \hbar\omega_{\text{input}}$ . In addition to quantum noise, the classical noise from the input laser

must be considered as well. Because the classical noise and the quantum noise are uncorrelated, we get

$$\langle \delta X_{\text{in}}(\omega)^2 \rangle = \hbar\omega_{\text{in}} + S_{\text{RIN}}(\omega)P_{\text{in}}, \quad (\text{C4a})$$

$$\langle \delta Y_{\text{in}}(\omega)^2 \rangle = \hbar\omega_{\text{in}} + S_{\xi}(\omega)P_{\text{in}}, \quad (\text{C4b})$$

where  $S_{\text{RIN}}(\omega)$  and  $S_{\xi}(\omega)$  are the relative intensity noise spectrum and the relative-phase-noise spectrum, respectively.

To deal with the nonlinear system, we first calculate the mean optical fields  $\alpha_{\text{cw}}, \alpha_{\text{ccw}}$  with Eq. (A7) and thus calculate the intensity difference  $D$ . We then turn to the frequency domain and expand Eq. (C2) to the first order of the fluctuation terms as

$$\begin{aligned} i\omega\delta a_m = & -\frac{\kappa}{2}\delta a_m + i\Delta_{\text{in}}\delta a_m + ig_{\text{th}}^s\alpha_m \\ & + ig_0\delta a_{m'} + i(R_{\text{th}}^c \pm iI_{\text{th}}^c)\alpha_{m'} \\ & + iM(2|\alpha_m|^2 + 2|\alpha_{m'}|^2)\delta a_m + iM\alpha_m^2\delta a_m^\dagger \\ & + i2M\alpha_m\alpha_{m'}\delta a_{m'}^\dagger + i2M\alpha_{m'}^*\alpha_m\delta a_{m'} \\ & + \sqrt{\kappa_{\text{in}}}\delta a_{m,\text{in}} + \sqrt{\kappa_l}\delta a_l + \sqrt{\kappa_{\text{out}}}\delta a_{m,\text{out}}. \end{aligned} \quad (\text{C5})$$

By solving these linear equations, we find the linear dependence of the variance of the intensity difference  $\langle |\delta D|^2 \rangle$  on the variances of fluctuations.

Last, we add the perturbation  $\varepsilon$  and do the above calculation again and we find the sensing signal  $\Delta D = D' - D$  and the variance of the sensing signal  $\langle |\delta(\Delta D)|^2 \rangle(\omega) = \langle |\delta D'|^2 \rangle(\omega) + \langle |\delta D|^2 \rangle(\omega)$  in the form of Eq. (4).

Although the noise spectrum of different noise sources  $S_{\text{RIN}}(\omega), S_{\xi}(\omega), S_{\text{th}}(\omega)$  depend highly on the microcavity and the laser used in the sensor, here we present a brief discussion on the frequency dependence of these noise sources. The frequency dependence of the thermorefractive noise spectrum in optical microcavities is a Lorentzian shape spectrum:  $S_{\text{th}}(\omega) \propto \Gamma_T/(\Gamma_T^2 + \omega^2)$ , where  $\omega$  is the noise frequency and  $\Gamma_T$  is the single-mode thermal decay rate. More detailed consideration of the thermorefractive noise can be done for specific cavity geometries, while the spectrum converges to the Lorentzian shape spectrum at high frequencies [57]. The relative intensity noise  $S_{\text{RIN}}(\omega)$  highly depends on the type of laser used in experiments, and a past measurement of a laser source used in optical microcavity sensing revealed a  $1/\omega^2$  dependence [13]. The relative phase noise  $S_{\xi}(\omega)$  can be related to the relative frequency noise by  $S_{\xi}(\omega) = S_f(\omega)/\omega^2$ , which simply gives  $S_{\xi}(\omega) \propto 1/\omega^2$  when considering white frequency noise alone. These results assure the validity of considering  $c_{\text{th}}, c_{\text{RIN}}$  in the realistic limit of  $\omega \ll \kappa$  while the frequency dependence of  $c_{\xi}(\omega)$  cannot be neglected. Nevertheless, the normalized noise spectrum  $S_i(\omega)$  is irrelevant to the sensing method, so that the SNR of different methods depend on the coefficient in  $c_i(\omega) \cdot S_i(\omega)$ . Therefore, here

we discuss only the coefficients  $c_i(\omega)$  to compare the SNR performance, instead of normalized noise spectrum  $S_i(\omega)$ .

- 
- [1] M. R. Foreman, J. D. Swaim, and F. Vollmer, Whispering gallery mode sensors, *Adv. Opt. Photonics* **7**, 632 (2015).
- [2] Y. Pei, R. Vogel, and C. Minelli, in *Characterization of Nanoparticles*, Micro and Nano Technologies, edited by V.-D. Hodoroaba, W. E. Unger, and A. G. Shard (Elsevier, Netherlands, Amsterdam, 2020), p. 117.
- [3] S. J. Sowerby, M. F. Broom, and G. B. Petersen, Dynamically resizable nanometre-scale apertures for molecular sensing, *Sens. Actuators B: Chem.* **123**, 325 (2007).
- [4] H. Bayley and C. R. Martin, Resistive-pulse sensing from microbes to molecules, *Chem. Rev.* **100**, 2575 (2000).
- [5] M. Wright, in *Encyclopedia of Nanotechnology*, edited by B. Bhushan (Springer Netherlands, Dordrecht, 2012), p. 1652.
- [6] R. A. Dragovic, C. Gardiner, A. S. Brooks, D. S. Tannetta, D. J. Ferguson, P. Hole, B. Carr, C. W. Redman, A. L. Harris, and P. J. Dobson *et al.*, Sizing and phenotyping of cellular vesicles using nanoparticle tracking analysis, *Nanomedicine: Nanotechnol. Biol. Med.* **7**, 780 (2011).
- [7] R. W. Taylor and V. Sandoghdar, Interferometric scattering microscopy: Seeing single nanoparticles and molecules via Rayleigh scattering, *Nano. Lett.* **19**, 4827 (2019).
- [8] J. Ortega-Arroyo and P. Kukura, Interferometric scattering microscopy (iscat): New frontiers in ultrafast and ultrasensitive optical microscopy, *Phys. Chem. Chem. Phys.* **14**, 15625 (2012).
- [9] M. Piliarik and V. Sandoghdar, Direct optical sensing of single unlabelled proteins and super-resolution imaging of their binding sites, *Nat. Commun.* **5**, 1 (2014).
- [10] S. Arnold, D. Keng, S. I. Shopova, S. Holler, W. Zurawsky, and F. Vollmer, Whispering gallery mode carousel - a photonic mechanism for enhanced nanoparticle detection in biosensing, *Opt. Express* **17**, 6230 (2009).
- [11] J. Zhu, S. K. Özdemir, Y.-F. Xiao, L. Li, L. He, D.-R. Chen, and L. Yang, On-chip single nanoparticle detection and sizing by mode splitting in an ultrahigh-Q microresonator, *Nat. Photon.* **4**, 46 (2010).
- [12] L. N. He, S. K. Özdemir, J. G. Zhu, W. Kim, and L. Yang, Detecting single viruses and nanoparticles using whispering gallery microlasers, *Nat. Nanotech.* **6**, 428 (2011).
- [13] J. Knittel, J. D. Swaim, D. L. McAuslan, G. A. Brawley, and W. P. Bowen, Back-scatter based whispering gallery mode sensing, *Sci. Rep.* **3**, 5 (2013).
- [14] L. B. Shao, X. F. Jiang, X. C. Yu, B. B. Li, W. R. Clements, F. Vollmer, W. Wang, Y.-F. Xiao, and Q. Gong, Detection of single nanoparticles and lentiviruses using microcavity resonance broadening, *Adv. Mater.* **25**, 5616 (2013).
- [15] Y. Y. Zhi, X. C. Yu, Q. Gong, L. Yang, and Y. F. Xiao, Single nanoparticle detection using optical microcavities, *Adv. Mater.* **29**, 19 (2017).
- [16] M. D. Baaske, M. R. Foreman, and F. Vollmer, Single-molecule nucleic acid interactions monitored on a label-free microcavity biosensor platform, *Nat. Nanotech.* **9**, 933 (2014).
- [17] F. Vollmer, S. Arnold, and D. Keng, Single virus detection from the reactive shift of a whispering-gallery mode, *Proc. Natl. Acad. Sci. U.S.A.* **105**, 20701 (2008).
- [18] J. Su, A. F. G. Goldberg, and B. M. Stoltz, Label-free detection of single nanoparticles and biological molecules using microtoroid optical resonators, *Light: Sci. Appl.* **5**, e16001 (2016).
- [19] M. D. Baaske and F. Vollmer, Optical observation of single atomic ions interacting with plasmonic nanorods in aqueous solution, *Nat. Photonics* **10**, 733 (2016).
- [20] B. Min, E. Ostby, V. Sorger, E. Ulin-Avila, L. Yang, X. Zhang, and K. Vahala, High-Q surface-plasmon-polariton whispering-gallery microcavity, *Nature (London)* **457**, 455 (2009).
- [21] Y.-F. Xiao, C.-L. Zou, B.-B. Li, Y. Li, C.-H. Dong, Z.-F. Han, and Q. Gong, High-Q Exterior Whispering-Gallery Modes in a Metal-Coated Microresonator, *Phys. Rev. Lett.* **105**, 153902 (2010).
- [22] Y.-F. Xiao, Y.-C. Liu, B.-B. Li, Y.-L. Chen, Y. Li, and Q. Gong, Strongly enhanced light-matter interaction in a hybrid photonic-plasmonic resonator, *Phys. Rev. A* **85**, 031805 (2012).
- [23] J. D. Swaim, J. Knittel, and W. P. Bowen, Detection of nanoparticles with a frequency locked whispering gallery mode microresonator, *Appl. Phys. Lett.* **102**, 183106 (2013).
- [24] J. Wiersig, Enhancing the Sensitivity of Frequency and Energy Splitting Detection by Using Exceptional Points: Application to Microcavity Sensors for Single-Particle Detection, *Phys. Rev. Lett.* **112**, 5 (2014).
- [25] J. Wiersig, Sensors operating at exceptional points: General theory, *Phys. Rev. A* **93**, 9 (2016).
- [26] H. Hodaei, A. U. Hassan, S. Wittek, H. Garcia-Gracia, R. El-Ganainy, D. N. Christodoulides, and M. Khajavikhan, Enhanced sensitivity at higher-order exceptional points, *Nature (London)* **548**, 187 (2017).
- [27] W. J. Chen, S. K. Özdemir, G. M. Zhao, J. Wiersig, and L. Yang, Exceptional points enhance sensing in an optical microcavity, *Nature (London)* **548**, 192 (2017).
- [28] W. J. Chen, J. Zhang, B. Peng, S. K. Özdemir, X. D. Fan, and L. Yang, Parity-time-symmetric whispering-gallery mode nanoparticle sensor (invited), *Photonics Res.* **6**, A23 (2018).
- [29] Y. H. Lai, Y. K. Lu, M. G. Suh, Z. Q. Yuan, and K. Vahala, Observation of the exceptional-point-enhanced sagnac effect, *Nature (London)* **576**, 65 (2019).
- [30] P. Djorwe, Y. Pennec, and B. Djafari-Rouhani, Exceptional Point Enhances Sensitivity of Optomechanical Mass Sensors, *Phys. Rev. Appl.* **12**, 10 (2019).
- [31] W. Langbein, No exceptional precision of exceptional-point sensors, *Phys. Rev. A* **98**, 8 (2018).
- [32] N. A. Mortensen, P. A. D. Goncalves, M. Khajavikhan, D. N. Christodoulides, C. Tserkezis, and C. Wolff, Fluctuations and noise-limited sensing near the exceptional point of parity-time-symmetric resonator systems, *Optica* **5**, 1342 (2018).
- [33] H. K. Lau and A. A. Clerk, Fundamental limits and non-reciprocal approaches in non-hermitian quantum sensing, *Nat. Commun.* **9**, 13 (2018).

- [34] M. Z. Zhang, W. Sweeney, C. W. Hsu, L. Yang, A. D. Stone, and L. Jiang, Quantum Noise Theory of Exceptional Point Amplifying Sensors, [Phys. Rev. Lett. \*\*123\*\*, 6 \(2019\)](#).
- [35] C. Chen, L. Jin, and R.-B. Liu, Sensitivity of parameter estimation near the exceptional point of a non-Hermitian system, [New J. Phys. \*\*21\*\*, 083002 \(2019\)](#).
- [36] H. Wang, Y.-H. Lai, Z. Yuan, M.-G. Suh, and K. Vahala, Petermann-factor sensitivity limit near an exceptional point in a Brillouin ring laser gyroscope, [Nat. Commun. \*\*11\*\*, 1610 \(2020\)](#).
- [37] J. A. Armstrong, N. Bloembergen, J. Ducuing, and P. S. Pershan, Interactions between light waves in a nonlinear dielectric, [Phys. Rev. \*\*127\*\*, 1918 \(1962\)](#).
- [38] Q.-T. Cao, H. Wang, C.-H. Dong, H. Jing, R.-S. Liu, X. Chen, L. Ge, Q. Gong, and Y.-F. Xiao, Experimental Demonstration of Spontaneous Chirality in a Nonlinear Microresonator, [Phys. Rev. Lett. \*\*118\*\*, 5 \(2017\)](#).
- [39] L. Del Bino, J. M. Silver, S. L. Stebbings, and P. Del'Haye, Symmetry breaking of counter-propagating light in a nonlinear resonator, [Sci. Rep. \*\*7\*\*, 43142 \(2017\)](#).
- [40] A. E. Kaplan and P. Meystre, Enhancement of the Sagnac effect due to nonlinearly induced nonreciprocity, [Opt. Lett. \*\*6\*\*, 590 \(1981\)](#).
- [41] C. Wang and C. P. Search, A nonlinear microresonator refractive index sensor, [J. Lightwave Technol. \*\*33\*\*, 4360 \(2015\)](#).
- [42] C. Wang and C. P. Search, Enhanced rotation sensing by nonlinear interactions in silicon microresonators, [Opt. Lett. \*\*39\*\*, 4376 \(2014\)](#).
- [43] J. M. Silver, L. Del Bino, M. T. Woodley, G. N. Ghalanos, A. Ø. Svela, N. Moroney, S. Zhang, K. T. Grattan, and P. Del'Haye, Nonlinear enhanced microresonator gyroscope, [Optica \*\*8\*\*, 1219 \(2021\)](#).
- [44] N. Moroney, L. D. Bino, M. T. M. Woodley, G. N. Ghalanos, J. M. Silver, A. Ø. Svela, S. Zhang, and P. Del'Haye, Logic gates based on interaction of counterpropagating light in microresonators, [J. Lightwave Technol. \*\*38\*\*, 1414 \(2020\)](#).
- [45] L. D. Bino, M. T. M. Woodley, J. M. Silver, S. Zhang, and P. Del'Haye, in *2018 Conference on Lasers and Electro-Optics (CLEO)*, p. 1.
- [46] M. T. M. Woodley, L. Hill, L. Del Bino, G.-L. Oppo, and P. Del'Haye, Self-Switching Kerr Oscillations of Counter-propagating Light in Microresonators, [Phys. Rev. Lett. \*\*126\*\*, 043901 \(2021\)](#).
- [47] L. Del Bino, J. M. Silver, M. T. M. Woodley, S. L. Stebbings, X. Zhao, and P. Del'Haye, Microresonator isolators and circulators based on the intrinsic nonreciprocity of the Kerr effect, [Optica \*\*5\*\*, 279 \(2018\)](#).
- [48] M. L. Gorodetsky, A. D. Pryamikov, and V. S. Ilchenko, Rayleigh scattering in high-Q microspheres, [J. Opt. Soc. Am. B \*\*17\*\*, 1051 \(2000\)](#).
- [49] T. J. Kippenberg, S. M. Spillane, and K. J. Vahala, Modal coupling in traveling-wave resonators, [Opt. Lett. \*\*27\*\*, 1669 \(2002\)](#).
- [50] A. Mazzei, S. Götzinger, L. de S. Menezes, G. Zumofen, O. Benson, and V. Sandoghdar, Controlled Coupling of Counterpropagating Whispering-Gallery Modes by a Single Rayleigh Scatterer: A Classical Problem in a Quantum Optical Light, [Phys. Rev. Lett. \*\*99\*\*, 173603 \(2007\)](#).
- [51] J. Zhu, S. K. Özdemir, L. He, and L. Yang, Controlled manipulation of mode splitting in an optical microcavity by two rayleigh scatterers, [Opt. Express \*\*18\*\*, 23535 \(2010\)](#).
- [52] B.-B. Li, W. R. Clements, X.-C. Yu, K. Shi, Q. Gong, and Y.-F. Xiao, Single nanoparticle detection using split-mode microcavity Raman lasers, [Proc. Natl. Acad. Sci. U.S.A. \*\*111\*\*, 14657 \(2014\)](#).
- [53] K. Ikeda, R. E. Saperstein, N. Alic, and Y. Fainman, Thermal and Kerr nonlinear properties of plasma-deposited silicon nitride/silicon dioxide waveguides, [Opt. Express \*\*16\*\*, 12987 \(2008\)](#).
- [54] F. Treussart, V. S. Ilchenko, J. F. Roch, J. Hare, V. Lefevre-Seguin, J. M. Raimond, and S. Haroche, Evidence for intrinsic Kerr bistability of high-Q microsphere resonators in superfluid helium, [Eur. Phys. J. D \*\*1\*\*, 235 \(1998\)](#).
- [55] B. Garbin, J. Fatome, G.-L. Oppo, M. Erkintalo, S. G. Murdoch, and S. Coen, Asymmetric balance in symmetry breaking, [Phys. Rev. Res. \*\*2\*\*, 023244 \(2020\)](#).
- [56] Y. Zheng, T. Qin, J. Yang, X. Chen, L. Ge, and W. Wan, Observation of gain spiking of optical frequency comb in a microcavity, [Opt. Express \*\*25\*\*, 31140 \(2017\)](#).
- [57] C. Panuski, D. Englund, and R. Hamerly, Fundamental Thermal Noise Limits for Optical Microcavities, [Phys. Rev. X \*\*10\*\*, 041046 \(2020\)](#).